**Sensing delamination in composites reinforced by ferromagnetic Z-pins via electromagnetic induction**

Bing Zhang[*], Stephen R. Hallett, Giuliano Allegri

Bristol Composites Institute, University of Bristol, Queen's Building, University Walk, Bristol BS8 1TR, UK

**Abstract**

This paper investigates a novel technique for sensing delamination in through-thickness reinforced composites based on electromagnetic induction. This sensing technique features ferromagnetic Z-pins and a pair of coils attached to a laminate; the first coil creates a magnetic field that is intensified by the ferromagnetic pins, whilst the second coil detects the magnetic flux change that is caused by the pin motion relative to the coil pair when delamination happens. This approach avoids potential interferences due to contact electrical resistances that exist in electrical-based sensing approaches. The viability of this sensing technique is demonstrated by monotonic and cyclic bridging tests, involving Nickel/Iron alloy Z-pins embedded in E-glass/913 laminates under controlled delamination. A simplified electromagnetic finite element analysis is presented to help interpret the experimental results. The sensitivity of the magnetic-based sensing technique increases with loading rate. Both mode I and mode II delamination events can be detected by a voltage signal from the sensing coil, albeit there exists an initial "blind spot" at low loading rates. This sensing technique also allows monitoring the pin bridging status, e.g. the switch of pin pull-out side, without modifications to the architecture of a Z-pinned composite regarding expected mechanical response.

*Corresponding author: b.zhang@bristol.ac.uk (Bing Zhang).

## 1. Introduction

Methods for enabling multifunctionality in fibre-reinforced plastic (FRP) have been attracting considerable research interest, because they can potentially broaden the engineering application of FRP composites, which are primarily employed due to their excellent specific mechanical properties. Non-load-carrying functions of FRP composites mainly involve sensing, actuation, energy harvesting, self-healing and electromagnetic interference shielding [1,2]. An FRP component itself can be considered multi-functional if it possesses adequate multi-physical properties. For example, a carbon FRP component can act as a self-health sensor as it is electrically conductive [3]. An alternative way of achieving multifunctionality for composites is by embedding a functional phase in the baseline material. Typical examples are carbon nanotube fillers, which offer both sensing and actuation functions [4].

Recently, there has been a growing interest in using discrete through-thickness reinforcement (TTR) elements, i.e. Z-pins, as a functional phase to offer an alternative means for enabling multifunctionality in composites, potentially because that Z-pins can be in principle made of any material that can be processed into small rods. Z-pinning has been widely proved to be a very effective TTR technology for pre-preg based composites [5] in static [6–8], fatigue [9,10] and dynamic loading regimes [11,12].

Regarding multifunctional Z-pinned composites, Zhang et al. [13] experimentally demonstrated the delamination self-sensing function of Z-pinned composites by monitoring the through-thickness electrical resistance (ER) of laminates between the surface-mounted electrodes connected to individual conductive pins. Zhang et al. [14] later extended this ER-based delamination sensing method to a structural-level design, where conductive Z-pins are connected both in series and in parallel via arrays of electrodes attached to the laminate surface. The health monitoring technique allows detecting the location and extent of interlaminar cracks. Pegorin et al. [15] proposed a different TTR-based delamination

monitoring method, which involves attaching a pair of measuring electrodes to the top and bottom surfaces in an un-pinned region of a laminate, rather than directly onto individual pins. Delamination was thus sensed by the ER change between the two surface electrodes, and the detection sensitivity was found to be dependent on the pin volume fraction and the pin conductivity. Grigoriou et al. [16] later extended the sensing method proposed in Ref. [15] to Z-pinned sandwich composites. More recently, Kadlec et al. [17] demonstrated the ER-based health monitoring approach in Z-pinned adhesive-bonded lap joints and found that the electrical resistances of pins correlated well with the fatigue dis-bond length. Gu et al. [18] demonstrated that the reinforcement effect of piezoelectric Z-pins can be in theory tailored by applying an external electrical load. It has also been proved that Z-pins can enhance the electrical [16,19], thermal [20,21] and magnetic [22] properties of composites.

The ER-based sensing techniques above are all effective and straightforward to implement. Contact ERs exist in an ER-based sensing method between electrodes and pin ends, between pins and laminate or between electrodes and laminate [13–17]. It is difficult to quantify these contact ERs, which may also significantly vary during mechanical loading, thus affecting sensitivity and accuracy. Aiming to advance the state of the art, this paper proposes a novel delamination sensing technique for Z-pinned composites based on electromagnetic induction. The sensing technique as introduced in Section 2 is not affected by contact ERs, since it is based on magnetic induction instead of ER. The main objective of this study is to prove the feasibility of the proposed technique and understand the associated sensing mechanisms via a coupon level set-up, which allows directly evaluating the sensing technique under a controlled delamination event, as discussed in Section 3. The coupon-level study provides the necessary knowledge for scaling up the technique towards structure-level applications where delamination propagates across individual pins, following the same development paths for the reinforcement [7,11,12,23,24] and ER-based sensing [13,14]

functions of Z-pins. Experimental results are provided in Section 4. Section 5 presents simplified electromagnetic (EM) modelling to help interpret the experimental results.

## 2. Sensing methodology

Enabling magnetic-field-based sensing in an FRP laminate requires: 1) generating a magnetic field; and 2) detecting the magnetic field variation based on electromagnetic induction. These requirements are here achieved by a pair of conductive coils that are attached to the laminate. One coil creates the magnetic field by carrying an electric current, whilst the second coil picks up the magnetic field change according to Faraday's law of induction [25]. Consequently, it is required to correlate delamination with the magnetic field variation, to convert a delamination event to a measurable electrical signal according to the usual design philosophy of sensors [26]. Delamination in an FRP composite is expected to have a negligible effect on the magnetic flux distribution, since traditional FRP composites have a permeability close to that of free space [22,27]. Thus, introducing a third phase with high magnetic properties into composites becomes essential for the sensing strategy to work. Here, ferromagnetic Z-pin is selected as the "magnetic enhancement" phase. Two major reasons are behind the choice: 1) Z-pin can be in principle made of any ferromagnetic material that can be processed into small rods, thus it is relatively easy to tailor the resulting magnetic properties [22], as it has also been demonstrated for the electrical and thermal properties of composites [16,19,20]; 2) enabling the delamination sensing function requires no modifications to the architecture of the Z-pinned composites in terms of expected mechanical response, and it implies no changes on the ensuing mechanical response. The ferromagnetic Z-pins link the magnetic field variation to delamination, as it will be demonstrated in this paper.

## 3. Experimental programme

### 3.1 Specimen preparation

Fig. 1a shows the specimen configuration used for studying the induction-based sensing technique. It consisted of a laminate reinforced by ferromagnetic Z-pins and a surface-mounted coil pair. The laminate was made of 64 E-glass/913 plies (Hexcel, UK) following the stacking sequence $[(0/90/-45/45)_3/(-45/45/90/0)_3//(0/90/-45/45)_5/(-45/45/90/0)_5]$, where '//' indicates a 16 μm PTFE release film. The PTFE insert was intentionally offset from the mid-plane to promote pin pull-out from the thin (top) sub-laminate, although the experiment observations presented later show that pin pull-out from the thick (bottom) sub-laminate also occurred. The laminate has a $30 \times 30$ mm$^2$ in-plane dimension and a thickness of 9.0 mm (3.4 mm and 5.6 mm for the thin and thick blocks, respectively). An array of 0.25 mm diameter Ni80/Fe20 alloy Z-pins (GoodFellow, UK) covering a $6.1 \times 6.1$ mm$^2$ area were inserted through the thickness of the laminate. The pin misalignment relative to the laminate thickness direction was measured based on the distance from the pin ends to the specimen edges, and the averaged pin misalignment angle was 4.7°. The magnetic properties of the Ni/Fe permalloy pin have been characterised in Ref. [22]. It has a high magnetic permeability and low coercivity [22,28–30]. Two Z-pin array patterns were tested, "5 × 5" array with 2% areal density and "3 × 3" array with 0.5% areal density. The laminate is bridged only by the ferromagnetic Z-pins at the release-film plane. This allows assessing the bridging action of Z-pins in a controlled delamination event, without the effect of interlaminar bonding [6–9,11,13,24].

Fig. 1b shows that the coil assembly consists of a pair of superposed and concentric coils, and a simple one-layer printed circuit board for electrical connections between coils and measurement devices. Each coil was made by winding 405 turns of 0.1 mm diameter, single-core and circular enamelled copper wires onto a nylon coil core, with the assistance of a lathe. The coil core was made using a CNC machine with accurate dimension control, and its relevant dimensions are shown in Fig. 1c. The coil core has negligible magnetic permeability

and electrical conductivity, so it has no influence on the magnetic field. It should be noticed from Fig. 1a that the coil assembly symmetrically sits on the pinning area of the thin sub-laminate, and the excitation coil is placed between the sensing coil and the laminate.

To manufacture the test specimens, a panel was first laid up using E-glass/913 prepreg, stacking plies on an aluminium plate. The alloy pins were carefully cut from a wire roll with scissors and then manually inserted through the entire thickness of the panel. To avoid the pin ends coming into contact with the top and bottom metal plates during cure, potentially causing significant Z-pin misalignment [31], 3 mm thick rubber sheets were placed on both sides of the panel. The whole assembly was then vacuum bagged and cured in an autoclave under a consolidation pressure of 7 bar, following the cycle: 1) heating up to 90 °C at the rate of 2 °C/minute, 2) holding for 155 minutes, 3) heating up to 125 °C at 2 °C/minute, 4) holding for 90 minutes, and 5) cooling down to room temperature. This cure cycle was adopted to prevent a too fast exothermic reaction and to keep the temperature under control within the thick plate. After cure, the rubber sheets were carefully peeled off. The protruding pin ends were carefully trimmed using a flush cutter to achieve a near-flush surface finish. This is different from what was required for the previously proposed ER-based sensing technique, where pins protruded from the laminate surface for electrical connection [13,14]. The panel was cut into individual coupons using a water-cooled diamond saw. The coil assembly was attached to each specimen using a double-side adhesive tape before test set-up.

**3.2 Experimental set-up**

Fig. 2a shows the whole experimental set-up. Mode I and mode II loadings, illustrated in Fig. 2b, were applied under displacement control via a calibrated Instron 8872 servo-hydraulic machine, with a 1 kN load cell for mode I and a 5 kN load cell for mode II. Mode I and mode II rigs are shown via exploded views in Fig. 3. The span of the loading rigs was intentionally designed to be large enough to avoid the possible influence of the loading

machine components on the magnetic field. The loading rigs were made of non-magnetic aluminium material. Mode I opening was applied to a specimen via two tabs, each of which was attached a pair of spacers. The specimen was sandwiched between the top and bottom spacers using cyanoacrylate universal superglue (Loctite Corp., UK). A cork block was inserted between the coil assembly and the loading tab, to help fix the coil pair. Mode II shear was also applied through two tabs, each of which was connected to an aluminium grip. These two grips have a matching rectangular slot. The specimen was carefully locked to the slot by a screw fastener on each grip, whilst lateral sliding was further suppressed by a pair of screw constraints on each side. The coil pair attaching to the thin sub-laminate was further supported by a tension-spring clamp, together with the double-side adhesive tape.

Regarding sensing measurement (referring to Fig. 2a), a 0.2 A DC current was injected into the excitation coil (recall Fig. 1a) via a TENMA 72-7245 power supply. The sensing coil was connected to a voltage amplifier with a $10^3$ gain and a bandwidth of 100 Hz. The voltage amplifier was further connected to a Tektronix TDS2024C digital oscilloscope for signal measurement. A NI/LabVIEW® programme was employed to record and synchronise the mechanical and sensing data. All the wires were properly fixed using electrical tape.

## 4. Experimental results

### 4.1 Mode I monotonic tests

Figs. 4a-b present the mode I monotonic test results of a "5 × 5" pin coupon and a "3 × 3" pin coupon. These two specimens were both loaded up to 9 mm. Displacement curves were measured by the loading machine, and velocity curves were obtained by the first derivative of the displacement curves. The opening velocity started from zero and rapidly increased to a value between 20 mm/s and 30 mm/s, then decreased to 20 mm/s in a nonlinear manner over a short period of time. The opening velocity was kept at 20 mm/s before it was rapidly reduced to zero. The load-cell readings were affected by inertia in the velocity build-up stage

[11], thus the load curves are not suitable for quantitively evaluating the bridging forces exerted by the alloy Z-pins. However, the following qualitative conclusions can be drawn.

1) The initial load spike was mainly due to inertia, although the pin/laminate bonding may also contribute to it. The 0.5% areal density specimen showed a negative load peak due to inertia. The microscopic observation of a carefully polished specimen surface in Fig. 5 shows no apparent pin/laminate interface cracking, but the post cure cool-down could weaken the interface due to the difference between the thermal expansion coefficients of the alloy Z-pins and the E-glass/913 laminate [8,32]. The mode II bridging results shown in the next sub-section will also confirm the existence of pin/laminate bonding.

2) The Nickel/Iron alloy pin showed a much lower peak bridging force than a T300/BMI composite Z-pin during the frictional pull-out stage [7]. This was expected, as metal Z-pins normally have a much smoother surface than fibrous (composite) ones [7,33].

3) Most pins experienced one-sided pull-out from either of the sub-laminate blocks, as summarised in Fig. 4c. For both specimens, one ("N") pin experienced double-sided pull-out, full pull-out from the top thin block and partial pull-out from the bottom thick block. The full pull-outs from the thin and thick sub-laminates, which are respectively marked by a vertical dashed line and a vertical solid line in Figs. 4a-b, were determined by the sub-laminate thicknesses, the displacement curves and load changes. All the pins were fully pulled out during the constant 20 mm/s loading stage.

Regarding the sensing results, background noise appeared in the sensing signal, but the signal-to-noise ratio was sufficiently high to identify key features. The loading onset was not clearly discernible in the voltage signals of both specimens, because the velocity was very small. Immediately after this short initial "blind phase", the voltage showed a sharp increase following the velocity trend, as indicated by black arrows in Figs. 4a-b. The voltage followed closely the velocity in the velocity build-up stage (up to around 0.08s) for the "5 × 5" pin

specimen, whilst it was less pronounced in the "3 × 3" pin specimen (up to around 0.04s).

In the subsequent constant 20 mm/s pull-out stage, the sensing signal showed a nonlinear decrease. The full pull-out of "B" pins from the thick sub-laminate was detected by a clear voltage drop in both tests, possibly because that the sudden loss of support from the thick sub-laminate pushed the "B" pins back towards the coils. When the velocity dropped to zero following the constant 20 mm/s pull-out stage, the voltage also became zero.

**4.2 Mode II monotonic tests**

Figs. 6a-b present the mode II monotonic test results. Note that "mode II" here indicates nominal mode II conditions, as a slight opening occurred between the top and bottom sub-laminates. The actual mode mixities (shear displacement divided by total displacement), measured by post-test corner pins, were 0.941 and 0.986 on average for the "5 × 5" and "3 × 3" specimens, respectively. The mode II displacement and velocity profiles were similar to those in mode I. The measured loads in the mode II tests were also affected by inertia, but qualitative observations can be also made regarding mode II bridging:

1) The initial load peak was dominated by Z-pin/laminate bonding and pin bending, with small contribution from inertial forces; this was confirmed by three "no-specimen" tests, which gave an inertial force not exceeding 12 N, more than ten times lower than the load peaks attained using the actual coupons; Z-pin/laminate debonding was accompanied by a clear load drop, although no load reversals were recorded.

2) After the initial drop, a clear load increase was observed, as indicated by black arrows in the load plots of Figs. 6a-b. This means that there was at least one pin that was already debonded from one of the sub-laminates at the load drop and that started debonding from the other sub-laminate. Subsequently, the load reached a plateau due to the plastic deformation of the metal pins, until a final rapid decrease took place due to the full pin pull-out [33].

3) All the mode II pins were fully pulled out from one sub-laminate without rupture, but

there was also partial pull-out from the other sub-laminate, as indicated in Fig. 6c. Most of the pins belonging to the "5 × 5" pin specimen were "N" pins. The "5 × 5" pin specimen also had four "K" pins, which were fully pulled out from the bottom thick sub-laminate, with partial pull-out from the top thin sub-laminate. All the pins belonging to the "3 × 3" pin specimen were "N" pins. The time instants corresponding to full pin pull-out from the thin and thick laminates, which were reflected by a clear load decrease, are respectively marked by a vertical dashed line in Fig. 6a and a vertical solid line in Figs. 6a-b.

4) After full pull-out, the load attained a non-zero value due to the pin ends scratching the release film and the sub-laminate from which it was pulled out, as seen in Fig. 7.

As in mode I, the initial short sensing "blind phase" occurring at low velocity also existed in mode II. Similarly, a sharp voltage increase immediately followed the blind phase also in the mode II tests, as indicated by black arrows in the voltage plots of Figs. 6a-b. The voltage signal followed closely the velocity curve in the velocity build-up stage, up to around 0.04s for both mode II specimens.

At the beginning of the constant-velocity stage, the voltage signal in both specimens showed an apparent increase (indicated by yellow arrows in Figs. 6a-b), in good correlation with the previously mentioned load increase occurring in this stage of the response (indicated by black arrows in the load plots of Figs. 6a-b). Subsequently, the sensing signal showed an overall nonlinear decreasing trend, as in mode I tests. The voltage dropped to zero when the pins were fully pulled out from the top thin sub-laminate.

## 4.3 Cyclic loading

To demonstrate the sensing technique under cyclic loading, two "5 × 5" pin specimens were tested in mode I and mode II, respectively. Firstly, the coupons were rapidly loaded up to 1 mm to achieve the mean displacement value for the cyclic step, where the specimens were loaded at 10 Hz for 100 cycles. In the third step, the specimens were loaded to full

failure at 0.5 mm/min. As in the velocity build-up stage observed in the monotonic tests, the sensing signals in the 1-mm steps of the cyclic tests (Figs. 8a-b) closely followed the velocity curves. The initial "blind phase" due to low velocity was also present in the 1-mm step, and the "blind phase" was larger for the mode II case, as shown in Fig. 8b.

Fig. 8c shows that the sensing signal in the mode I cyclic step agreed closely with the velocity profile and the signal amplitude increased with velocity. In the mode II cyclic step, the sensing signal followed closely the velocity curve for the first 11 cycles. Z-pin failure caused a decrease in signal amplitude during the 4th cycle, as indicated by an arrow in Fig. 8d. Between the 12th to 15th cycles, the remaining active pins were progressively broken. The voltage signal became distorted and hard to identify after the 12th cycle. This could be due to: 1) the scratching of pin broken ends onto the release film, which periodically drags the TTR rods in and out the embedded blocks; 2) pin debris sliding between the two sub-laminates during cyclic loading; and 3) the horizontal motion of the bottom pin segments embedded into the thick sub-laminate with respect to the coil pair, which also contributed to the signal, as it will be discussed later. The third step showed no sensing signal due to the quasi-static loading rate. Fig. 8e gives the failure status of each mechanically cycled pin.

In addition, an un-pinned specimen was tested for all the loading cases described above, and no resulting sensing signal was detected. This means that the sensing signals were entirely due to the presence of the ferromagnetic Z-pins.

## 5. Discussion

Electromagnetic finite element analyses were performed in COMSOL Multiphysics® 5.5 to help explain the experimental results and unveil involved sensing mechanisms. Note that it is beyond the scope of this study to build multi-physical models by considering both pin bridging and EM induction. However, as it is shown below, the simplified EM models are very beneficial for understanding the mechanisms governing the sensing technique.

**5.1 Electromagnetic modelling**

In the EM modelling, each pin was assumed to be perfectly straight. As an example, Fig. 9a shows the "3 × 3" pin model. The coils were described by assuming a homogenised current flowing through their coil cross section in the circumferential direction, and the equivalent current density was set equal to the total current divided by the cross-section area [34]. The glass FRP laminate and the coil nylon core have a permeability close to that of free space [27], thus it was not necessary to include those in the model. The whole virtual specimen was enclosed in a 60 mm radius free-space sphere, which was verified to be sufficiently large to capture the magnetic flux distribution surrounding the virtual specimen. Hexahedral elements were used for the pins, and tetrahedral elements were used for the remaining parts of the model. A mesh convergence study was carried out for the model to ensure the robustness of the results. The "magnetic fields" interface in COMSOL was used to create a virtual magnetic field **H** based on Ampere's law: $\nabla \times \mathbf{H} = \mathbf{J}$, whereby **J** is the current density. The degree of freedom resolved for each element was the vector magnetic potential **A**, which is related to the magnetic flux density **B** by $\mathbf{B} = \nabla \times \mathbf{A}$.

The material B-H curve as verified in Ref. [22] was used for the alloy pins, and it is plotted in Fig. 9b. The excitation coil was loaded with 0.2 A DC current as in experiments. 0 A was input into the sensing coil to achieve an open-circuit voltage, considering that the amplifier used in experiments had a very high input impedance compared to the sensing coil. The open-circuit voltage V was computed based on Faraday's law of induction [25]:

$$V = \frac{d\lambda}{dt} = \sum_{i=1}^{N_s} \frac{-d \int_S \mathbf{B} \cdot d\mathbf{S_i}}{dt} \tag{1}$$

where $\lambda$ is the total magnetic flux concatenated by the sensing coil; $N_s$ is the number of turns in the sensing coil; $\mathbf{S_i}$ is the surface bounded by the i-th turn of the sensing coil. The predicted voltage was increased by 1000 and filtered by a second-order lowpass digital Butterworth filter to consider the gain and bandwidth of the amplifier used in experiments.

**5.2 Mode I**

The mode I monotonic tests were simply modelled by assuming that all the pins behaved as rigid bodies. The top-side pull-out pins (i.e. "T" pins in Fig. 4c) in the models moved away from the coils by following the experimental displacement curves (Figs. 4a-b) as rigid bodies. The "B" pins and the remaining parts of the models were fixed. The remeshing function in COMSOL was used to avoid element distortion. As the specimens both had one double-side pull-out "N" pin (recall Fig. 4c), two extreme scenarios, pull-out only from the top sub-laminate (as a "T" pin) and pull-out only from the bottom sub-laminate (as a "B" pin), were considered for the "N" pins in the models.

*Model verification*

Fig. 10 shows that the numerical results correlate well with experimental measurements on the overall trend of the sensing signals, even with the simplifications. Most importantly, the voltage increase at the early stage of the mode I tests was also captured by the models. The signal overestimation for the subsequent loading up to around 0.04 s (indicated by black arrows in Figs.10a-b) was due to the rigid pin assumption. In experiments all the pins deformed and gradually experienced deformation from their bottom ends to top ends due to the combination of the bonding and friction between pins and the laminate [6,8,33].

Except for the voltage drops due to full "B" pins pull-out from the bottom sub-laminates, the model predictions correlate very well with experiments during the stable frictional pull-out stage, which started from around 0.04s for the "5 × 5" pin specimen (indicated by a black arrow in Fig. 10a) and 0.05s for the "3 × 3" pin specimen (by a yellow arrow in Fig. 10b), respectively. Thus, the rigid pin assumption has minor influence on the model prediction accuracy during the frictional pull-out stage. The voltage jump observed in the "3 × 3" pin experimental sensing signal (between the black arrow and the yellow arrow in Fig. 10b) was due to the shift of the "N" pin from bottom-laminate pull-out to top-laminate pull-out. This is

revealed by comparing the two voltage curves that were respectively predicted with the two extreme assumptions for the "N" pin in Fig. 10b. There is very minor difference between the two "5 × 5" model curves because the "T" pins fully dominated the sensing signal. Hence, it is hard to tell when the "N" pin of the "5 × 5" pin specimen shifted its pull-out side.

The FE models also allow observing the decrease of the magnetic flux concatenated by the sensing coil when the "T" pins moved away from the coil pair, as shown in Fig. 11 by the "5×5" pin model result with the "N" pin fixed throughout. The magnetic flux density norms of the pins at selected time instants are shown in the inset figures of Fig. 11, whereby the maximum and minimum flux values are listed near triangle symbols. As the "T" pins moved away from the coil pair, the magnetic flux density inside the "T" pins decreased. It also affected the flux density distribution inside the "B" pins, and the maximum of the "B" pin flux density norm showed an increasing trend with the "T" pin pull-out.

*Sensing mechanisms*

Considering the numerical and experimental results as a whole, it can now be confirmed that the mode I sensing signal was mainly due to the vertical motion of the pins relative to the coil pair. Before the frictional pull-out stage was attained, the relative motion with respect to the coils involved all pins because of pin/laminate bonding and friction. During the frictional pull-out stage, the relative motion would be experienced by the "T" pins, as well as the "N" pin if it started to be pulled out from the top sub-laminate. Also, according to Faraday's law of induction (Eq. 1), the sensing signal is proportional to the pin velocity, whilst for a constant velocity the sensing signal decreases as the sensing pin moves away from the coil pair. The pins had less effect on the magnetic field when moving further from the excitation coil, thus the sensing signal gradually decreased with loading, as observed in the tests. This is also the reason why the crack closure (negative velocity) at the end of the tests was not detected since the sensing pins were sufficiently far away from the coils.

Based on the analyses above, more information can also be gathered from the mode I cycles test results. For instance, an apparent reduction of the sensing signal amplitude, indicated by an arrow in Fig. 8c, is likely due to the decrease of the number of "T" pins.

**5.3 Sensing mechanisms in Mode II**

In mode II, pin pull-out also happened due to the ductility of the metal pins [6,33]. Full pin pull-out was observed for all the mode II monotonic pins. Thus, the vertical pin motion relative to coils also contributed to mode II sensing signal. Like in mode I, the change of pin pull-out side can also be sensed in mode II, as it is indicated by yellow arrows in Figs. 6a-b.

The pin segments embedded within the bottom thick sub-laminate may also contribute to the signal, since they showed horizontal motion relative to the coils. To examine this effect, the "3 × 3" pin model was employed. The top pin segments that correspond to the length embedded in the top sub-laminate of the specimen were fixed, whilst the bottom pin segments moved in the horizontal direction following the experimental displacement curve shown in Fig. 6b. A 1 mm transition length following a simple smoothing function was assumed between the top and bottom pin parts to avoid cutting off the virtual pins. To study the effect of horizontal pin motion in isolation, the vertical pin motion was constrained in the model. This implies that the pin length in the model would increase due to the presence of the transition length, therefore only a small displacement (1 mm) was allowed in the model.

Fig. 12a shows that the horizontal pin motion also changes the magnetic flux through the pick-up coil, but it gives opposite effect compared to vertical pin motion (recall Fig. 11). The inset images in Fig. 12a shows that the horizontal pin motion only slightly affects the flux density distribution inside the pins compared to the vertical pin motion (recall Fig. 11). Comparing the "3 × 3" pin experimental signal in Fig. 6b and the modelling result in Fig. 12b, the mode II sensing signal up to 0.05s (1 mm displacement) was also dominated by the vertical pin motion, with much less contribution from the horizontal pin motion. The effects

of these two motion types on the mode II signal after 0.05 s should be further addressed with multi-physical simulations, that are in progress. However, it is guaranteed that the horizontal pin motion would not lead to a sensing signal when the pins were fully pulled out from the top thin sub-laminate, since the measured voltage became zero as shown in Figs. 6a-b.

## 5.4 Remarks

*Effect of pin misalignment*

Due to Z-pin misalignment, horizontal motion occurs even in mode I loading [8], and this can in principle influence the sensing signal. However, because the pin misalignment was small in this study, the pin horizontal motion due to pin misalignment has a minor effect on the mode I sensing signals presented in Figs. 4a-b compared to the vertical pin motion. This is further supported by the previous analysis that even for mode II loading up to 1 mm horizontal pin motion, the mode II sensing signal was still dominated by vertical pin motion.

*0.5 mm diameter Z-pin tests*

We also tested 0.5 mm diameter Ni80/Fe20 Z-pins pinned E-glass/913 specimens under mode I and mode II monotonic loadings, using the same experimental set-up and laminate configuration as described in Section 3. Two Z-pin array patterns, namely "3 × 3" and "2 × 2", were considered for the 0.5 mm pin tests. The sensing signals in the 0.5 mm pin tests have a very similar profile as the ones in the 0.25 mm pin tests. The typical sensing behaviours as analysed above for the 0.25 mm pin specimens were also observed in the 0.5 mm pin tests, e.g. the initial voltage increase, the voltage-velocity synchronisation during the velocity build-up stage and the non-linear voltage decrease during the constant-velocity stage. To save space, interested readers are referred to the Supplementary Material for more details about the larger pin test results.

*Effect of Z-pin array design*

Both the experiments and the simulations prove that the sensitivity of the magnetic-based

sensing method, which corresponds to the initial voltage peak, is determined by the number of "T" pins, assuming that a "N" pin starts pull-out from the coil-attached side of the laminate after the voltage peak if it exists. Hence, specimens comprising Z-pin arrays (and not just single Z-pins) were designed and tested to achieve a sufficient number of pins that were pulled out from the coil-attached side. Because that the pin/laminate interface is different between pins, the number of "N" pins may not be directly proportional to the number of Z-pins that are covered by the coils. This is supported by the observation that the number of "T" pins in the mode I "3 × 3" 0.5 mm pin specimen was smaller than the mode I "2 × 2" 0.5 mm pin specimen (refer to the Supplementary Material), thus the detection sensitivity was lower in the former than in the latter. However, the detection sensitivity increased with the number of the coil covered pins in other test cases. Therefore, it is not easy to draw a definite relationship between the number of Z-pins covered by the coils and the detection sensitivity.

*Comparison with ER-based Z-pin sensing methods*

It is hard to establish a direct comparison between the ER-based delamination sensing techniques [13–17] and the magnetic-based technique proposed here, because different experimental conditions were considered regarding loading rate, Z-pin material and specimen configuration. As explained above, the magnetic-based sensing technique is unaffected by contact ERs and this represents an advantage. The magnetic-based approach is particularly suited to high-loading-rate regimes. However, the effect of loading rate on the ER-based sensing methods has not been studied [13–17]. On the other hand, the magnetic-based method is not suitable for quasi-static conditions, for which however an ER-based sensing technique can be employed. In comparison with the ER-based method that was previously proposed by the authors [13,14], which requires Z-pins protruding from the laminate surfaces for electrode connection, the magnetic-based sensing technique requires no modifications to the architecture of the Z-pinned laminate. This implies that the magnetic-based sensing

approach can also be used as an in-situ technique to monitor the pin bridging behaviour.

## 6. Conclusions

This paper has presented a novel delamination sensing technique based on the magnetic field variation induced by ferromagnetic TTR in composites. The sensing approach requires a pair of superposed and concentric coils attached to a laminate; the first creates a magnetic field, while the second senses delamination by outputting a measurable electrical signal. The sensing method has been demonstrated and validated via mode I and mode II tests performed on E-glass/913 FRP specimens, reinforced with Nickel/Iron alloy Z-pin arrays.

The experimental results demonstrate that mode I and mode II delamination events can be clearly detected from the output voltage. The switch of pin pull-out side can be sensed as a voltage signal change. Z-pin rupture due to mode II loading could also be detected as a sudden signal drop. The voltage signal followed closely the velocity profile if no pin rupture, thus the sensitivity is proportional to loading rate. Preliminary EM modelling was used to help understand in depth the sensing mechanisms. The sensing signal was dominated by the Z-pins that showed relative vertical motion to the coil pair, although in mode II the sliding of Z-pin segments relative to the coil pair also played a role. As the sensing pins moved away from the coils, they showed reduced effect on the sensing coil concatenated flux, thus the sensing signal amplitude decreased.

The sensing method requires that the coil pair be attached at the same location on the laminate, so that the resulting sensing signal is fully caused by the Z-pin movement and deformation. If the coils were arranged at two different locations, the deformation of the laminate during loading would lead to a relative motion between the coils and thus a signal, which makes it hard to recognise delamination. Scaling up this sensing approach to structural level requires that the coils can conform to surface deformations, thus a multilayer copper-clad laminate sheet could be used to make the coil pair more compliant [35]. The structural-

level characterisation and application of the sensing technique proposed here will be reported in a separate paper.

## Acknowledgements

## References

[1]     R.F. Gibson, A review of recent research on mechanics of multifunctional composite materials and structures, Compos. Struct. 92 (2010) 2793–2810.

[2]     D.D.L. Chung, A review of multifunctional polymer-matrix structural composites, Compos. Part B Eng. 160 (2019) 644–660.

[3]     J.H. Kim, P.S. Shin, D.J. Kwon, J.M. Park, 2D electrical resistance (ER) mapping to Detect damage for carbon fiber reinforced polyamide composites under tensile and flexure loading, Compos. Sci. Technol. 201 (2021).

[4]     C. Li, E.T. Thostenson, T.-W. Chou, Sensors and actuators based on carbon nanotubes and their composites: A review, Compos. Sci. Technol. 68 (2008) 1227–1249.

[5]     A.P. Mouritz, Review of z-pinned laminates and sandwich composites, Compos. Part A Appl. Sci. Manuf. 139 (2020) 106128.

[6]     D.D.R. Cartié, B.N. Cox, N.A. Fleck, Mechanisms of crack bridging by composite and metallic rods, Compos. Part A Appl. Sci. Manuf. 35 (2004) 1325–1336.

[7]     M. Yasaee, J.K. Lander, G. Allegri, S.R. Hallett, Experimental characterisation of mixed mode traction–displacement relationships for a single carbon composite Z-pin, Compos. Sci. Technol. 94 (2014) 123–131.

[8]     B. Zhang, G. Allegri, M. Yasaee, S.R. Hallett, Micro-mechanical finite element analysis of Z-pins under mixed-mode loading, Compos. Part A Appl. Sci. Manuf. 78 (2015) 424–435.

[9]     F. Warzok, G. Allegri, M. Gude, S.R. Hallett, Experimental characterisation of fatigue damage in single Z-pins, Compos. Part A Appl. Sci. Manuf. 91 (2016) 461–471.

[10]    S. Tang, S. Lemanski, X. Zhang, D. Ayre, Fatigue life prediction of z-fibre pinned composite laminate under mode I loading, Compos. Sci. Technol. 174 (2019) 221–231.

[11]    H. Cui, M. Yasaee, S.R. Hallett, I.K. Partridge, G. Allegri, N. Petrinic, Dynamic bridging mechanisms of through-thickness reinforced composite laminates in mixed mode delamination, Compos. Part A Appl. Sci. Manuf. 106 (2018) 24–33.

[12]    M. Yasaee, G. Mohamed, A. Pellegrino, N. Petrinic, S.R. Hallett, Strain rate dependence of mode II delamination resistance in through thickness reinforced laminated composites, Int. J. Impact Eng. 107 (2017) 1–11.

[13]    B. Zhang, G. Allegri, M. Yasaee, S.R. Hallett, I.K. Partridge, On the delamination self-sensing function of Z-pinned composite laminates, Compos. Sci. Technol. 128 (2016) 138–146.

[14]    B. Zhang, G. Allegri, S.R. Hallett, An experimental investigation into multi-functional

Z-pinned composite laminates, Mater. Des. 108 (2016) 679–688.

[15]   F. Pegorin, K. Pingkarawat, A.P. Mouritz, Electrical-based delamination crack monitoring in composites using z-pins, Compos. Part A Appl. Sci. Manuf. 104 (2017) 120–128.

[16]   K. Grigoriou, R.B. Ladani, A.P. Mouritz, Electrical properties of multifunctional Z-pinned sandwich composites, Compos. Sci. Technol. 170 (2019) 60–69.

[17]   M. Kadlec, R. Růžek, P. Bělský, Concurrent use of Z-pins for crack arrest and structural health monitoring in adhesive-bonded composite lap joints, Compos. Sci. Technol. 188 (2020) 107967.

[18]   B. Gu, H. Zhang, B. Wang, S. Zhang, X. Feng, Fracture toughness of laminates reinforced by piezoelectric z-pins, Theor. Appl. Fract. Mech. 77 (2015) 35–40.

[19]   F. Pegorin, K. Pingkarawat, A.P. Mouritz, Controlling the electrical conductivity of fibre-polymer composites using z-pins, Compos. Sci. Technol. 150 (2017) 167–173.

[20]   F. Pegorin, K. Pingkarawat, A.P. Mouritz, Numerical analysis of the heat transfer properties of z-pinned composites, Compos. Commun. 8 (2018) 14–18.

[21]   M. Li, Z. Fang, S. Wang, Y. Gu, Y. Li, Z. Zhang, Thermal conductivity enhancement and heat transport mechanism of carbon fiber z-pin graphite composite structures, Compos. Part B Eng. 172 (2019) 603–611.

[22]   M. Chen, B. Zhang, S. Friedemann, G. Allegri, S.R. Hallett, Effects of ferromagnetic & carbon-fibre Z-Pins on the magnetic properties of composites, Compos. Sci. Technol. 207 (2021) 108749.

[23]   G. Mohamed, G. Allegri, M. Yasaee, S.R. Hallett, Cohesive element formulation for z-pin delamination bridging in fibre reinforced laminates, Int. J. Solids Struct. 132–133 (2018) 232–244.

[24]   K. Pingkarawat, A.P. Mouritz, Comparative study of metal and composite z-pins for delamination fracture and fatigue strengthening of composites, Eng. Fract. Mech. 154 (2016) 180–190.

[25]   M.N.O. Sadiku, Elements of electromagnetics, 3rd ed., Oxford University Press, 2001.

[26]   J. Fraden, Handbook of Modern Sensors: Physics, Designs, and Applications, 4th Editio, Springer, 2010.

[27]   J. Etches, I. Bond, P. Mellor, Manufacture and applications of magnetically active fibre reinforced composites, Smart Mater. Struct. 15 (2006) 288–294.

[28]   H.D. Arnold, G.W. Elmen, Permalloy, a new magnetic material of very high permeability, Bell Syst. Tech. J. 2 (1923) 101–111.

[29]   D. Jiles, Introduction to magnetism and magnetic materials, 3rd ed., CRC Press, 2015.

[30]   M. Mirzaei, P. Ripka, Analytical functions of magnetization curves for high magnetic permeability materials, IEEE Trans. Magn. 54 (2018).

[31]   D.D.R. Cartié, J.M. Laffaille, I.K. Partridge, A.J. Brunner, Fatigue delamination behaviour of unidirectional carbon fibre/epoxy laminates reinforced by Z-Fiber® pinning, Eng. Fract. Mech. 76 (2009) 2834–2845.

[32]   R.D. Sweeting, R.S. Thomson, The effect of thermal mismatch on Z-pinned laminated composite structures, Compos. Struct. 66 (2004) 189–195.

[33]   B. M'membe, M. Yasaee, S.R. Hallett, I.K. Partridge, Effective use of metallic Z-Pins for composites' through-thickness reinforcement, Compos. Sci. Technol. 175 (2018) 77–84.

[34]   M. Duhovic, L. Moser, P. Mitschang, M. Maier, I. Caldichoury, P. L'Eplattenier, Simulating the joining of composite materials by electromagnetic induction, in: Proc. 12th Int. LS-DYNA® Users Conf., Detroit, 2012.

[35]   J.S. Chilles, A. Croxford, I.P. Bond, Design of an embedded sensor, for improved structural performance, Smart Mater. Struct. 24 (2015) 115014 (10pp).
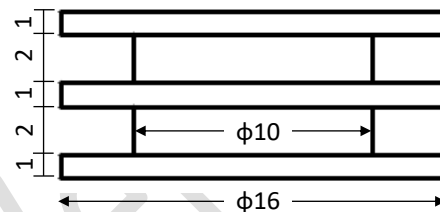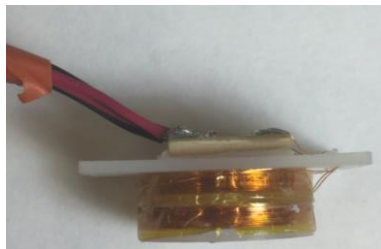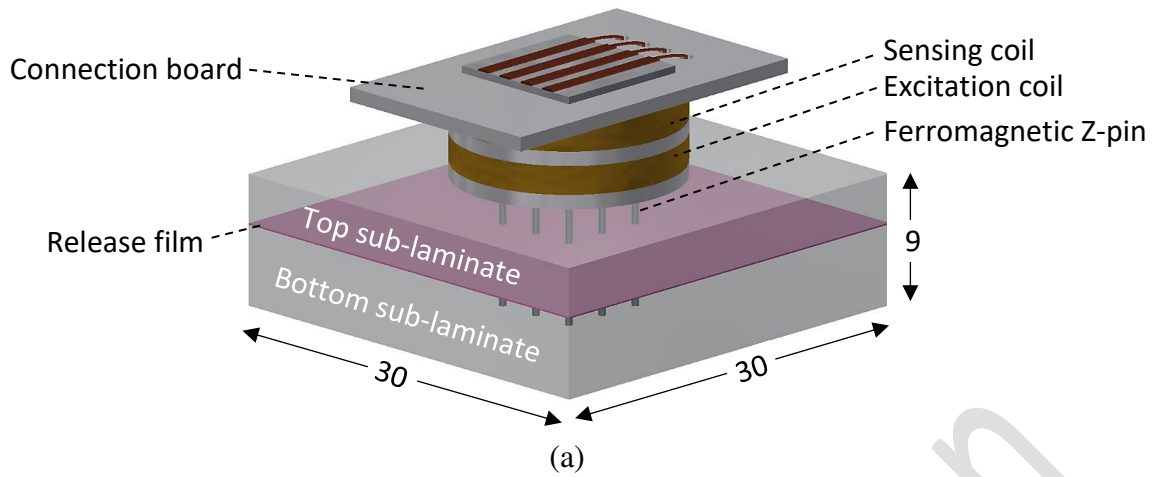
Fig. 1. (a) Specimen configuration used for demonstrating the sensing technique, (b) the coil assembly used in this study and (c) the critical dimensions of the coil core (unit: mm).
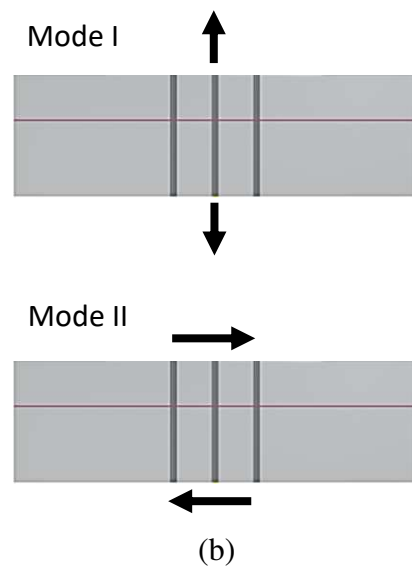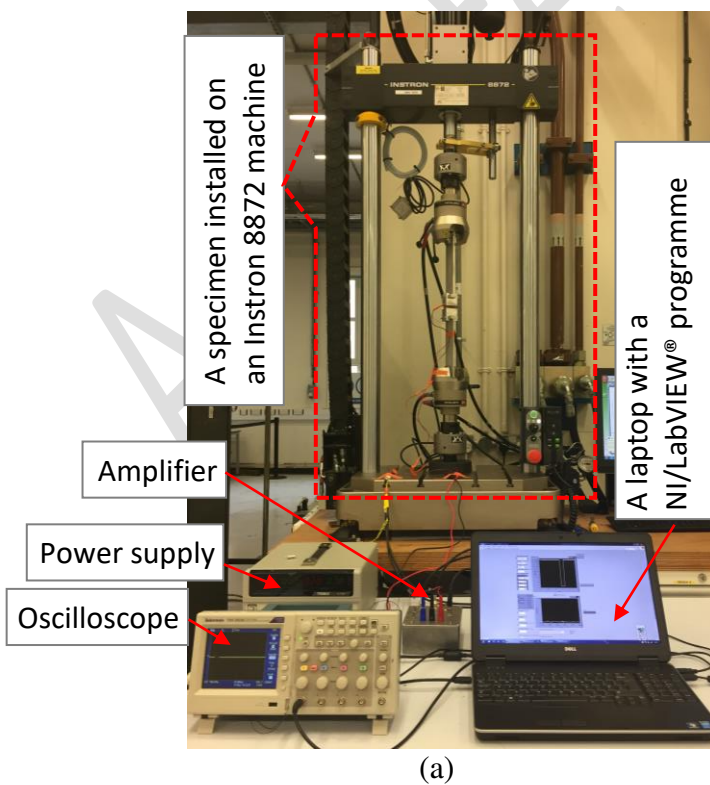


Fig. 2. (a) Experimental set-up, and (b) schematic diagrams of mode I and mode II loadings.
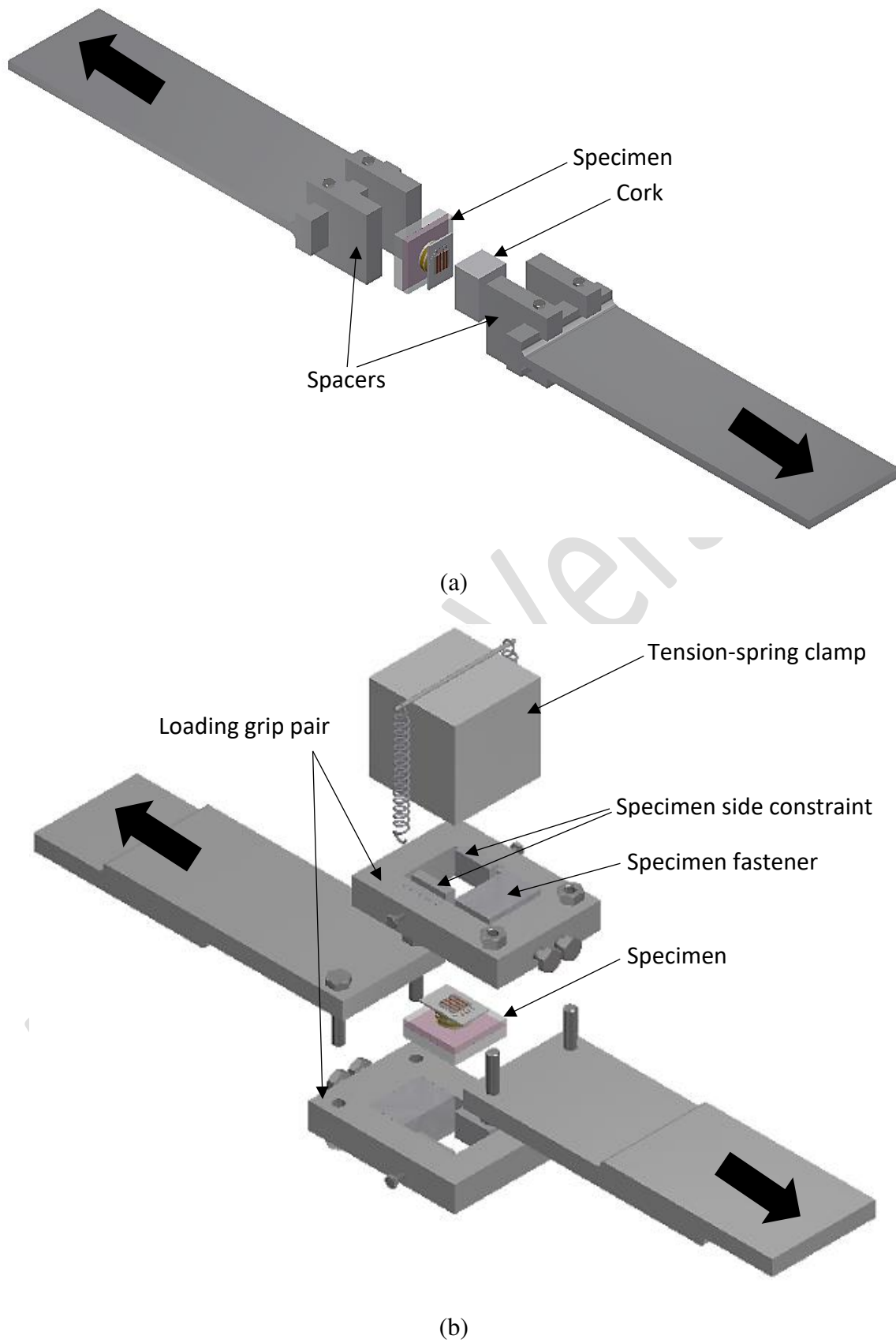
(a)



(b)

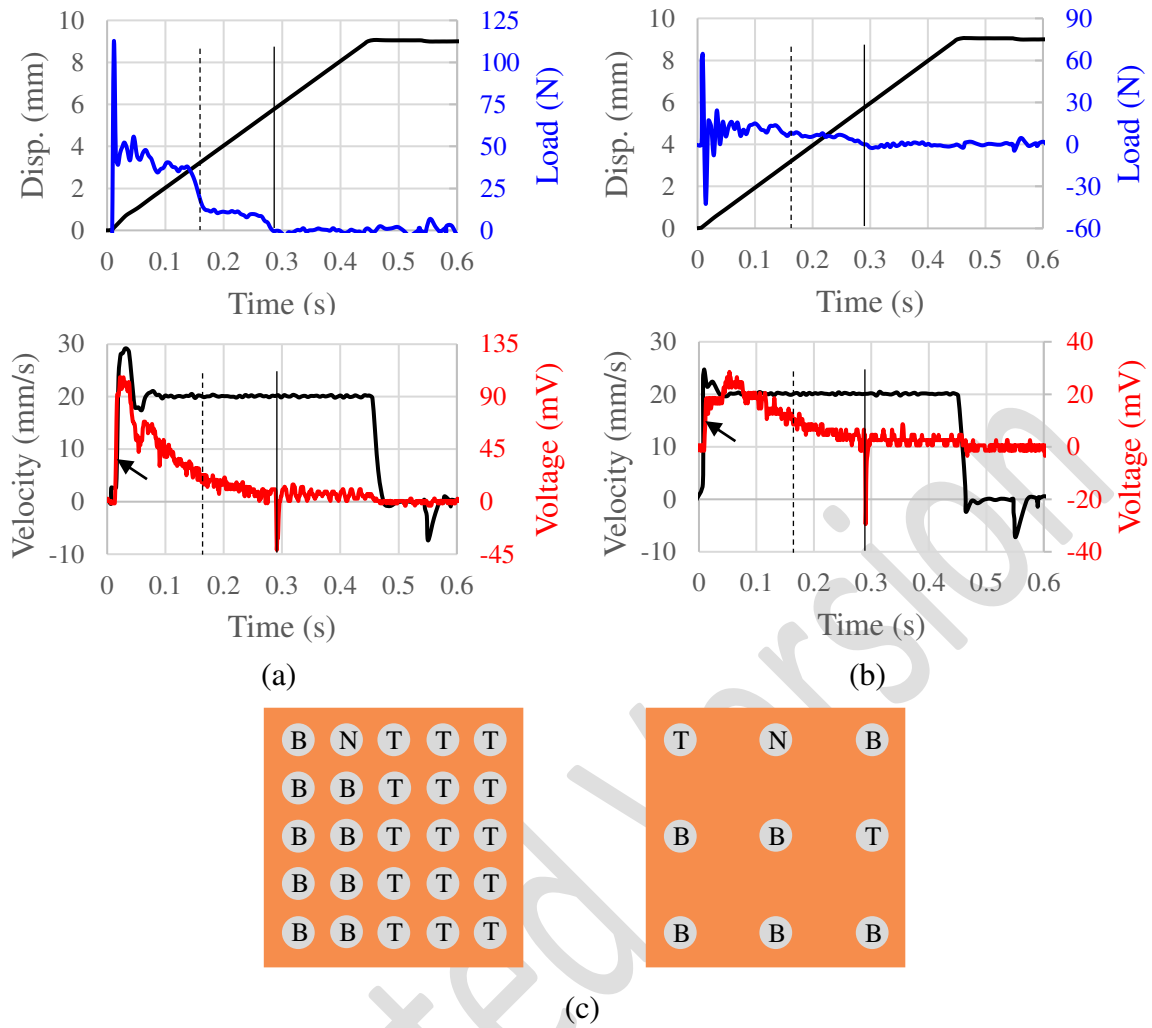Fig. 3. Exploded views of (a) mode I and (b) mode II test rigs.

(a)

(b)

(c)

Fig. 4. Mode I monotonic results of (a) a "5 × 5" pin specimen and (b) a "3 × 3" pin specimen; (c) plot of pin pull-out side, whereby "T" means pull-out from top thin block, "B" pull-out from bottom thick block, and "N" pull-out from thin block and partial pull-out from thick block.
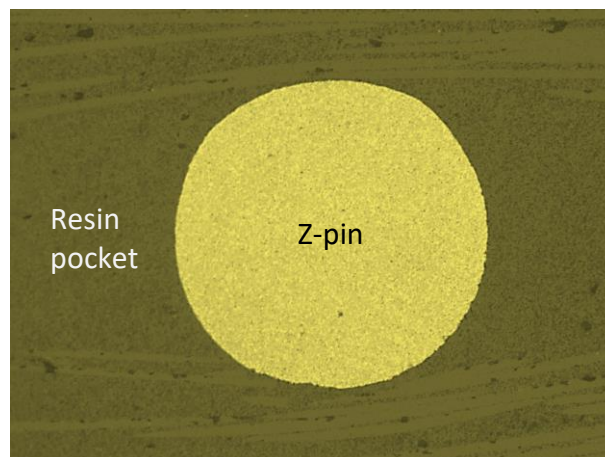


Fig. 5. Microscopic observation of a carefully polished specimen surface.

(a)                                                (b)



(c)
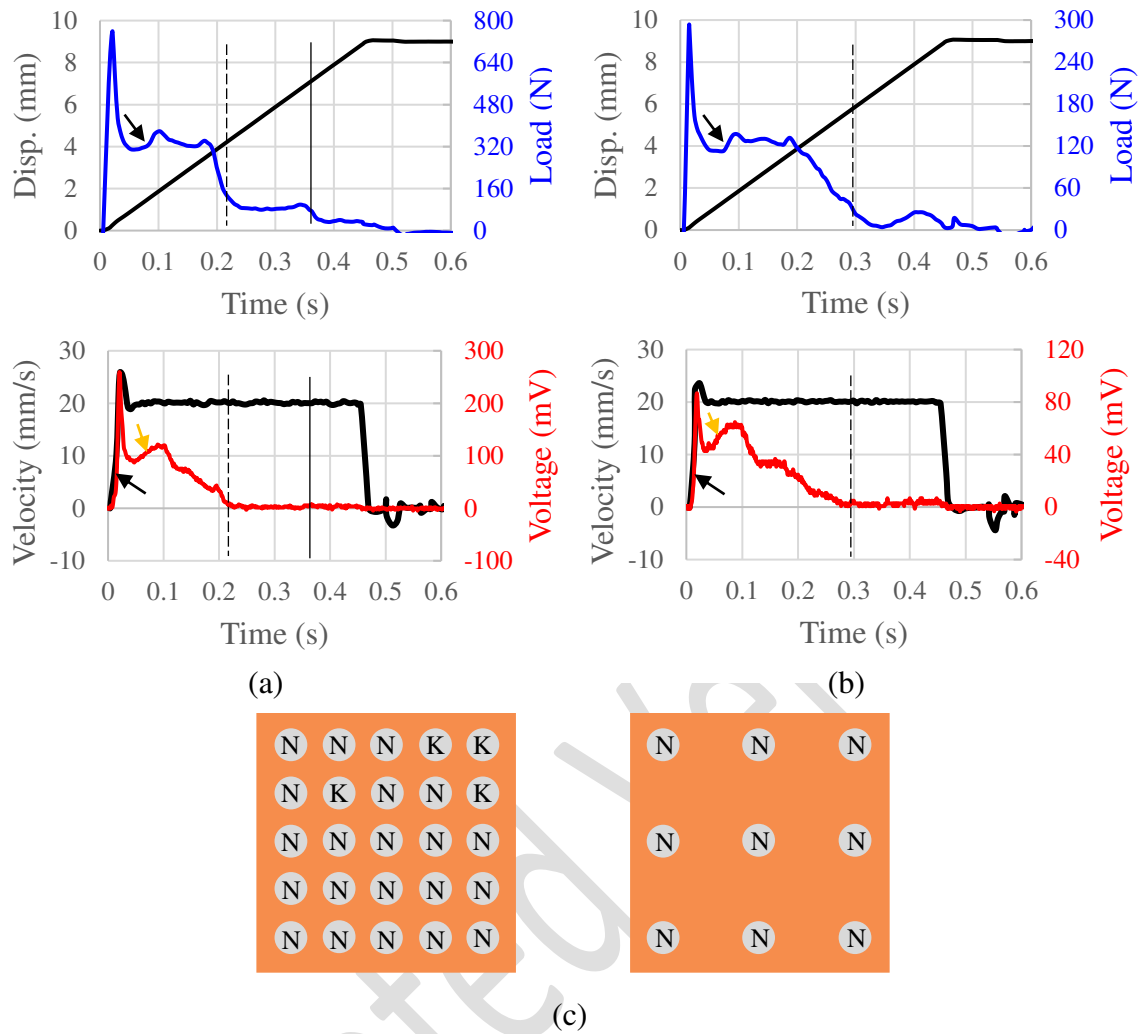
Fig. 6. Mode II monotonic results of (a) a "5 × 5" pin specimen and (b) a "3 × 3" pin specimen; (c) plot of pin pull-out side, whereby "N" means pull-out from thin block and partial pull-out from thick block, and "K" pull-out from thick block and partial pull-out from thin block.
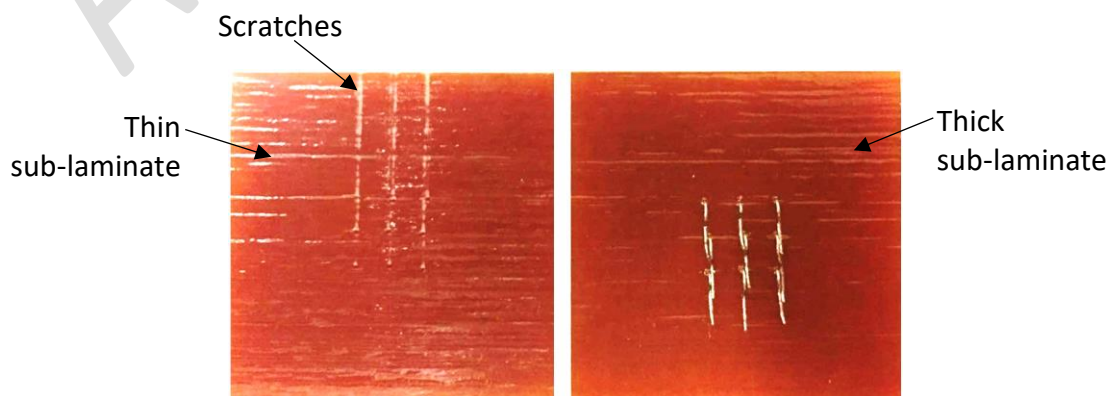


Fig. 7.  Post-test observation of the mode II monotonic "3 × 3" pin specimen.
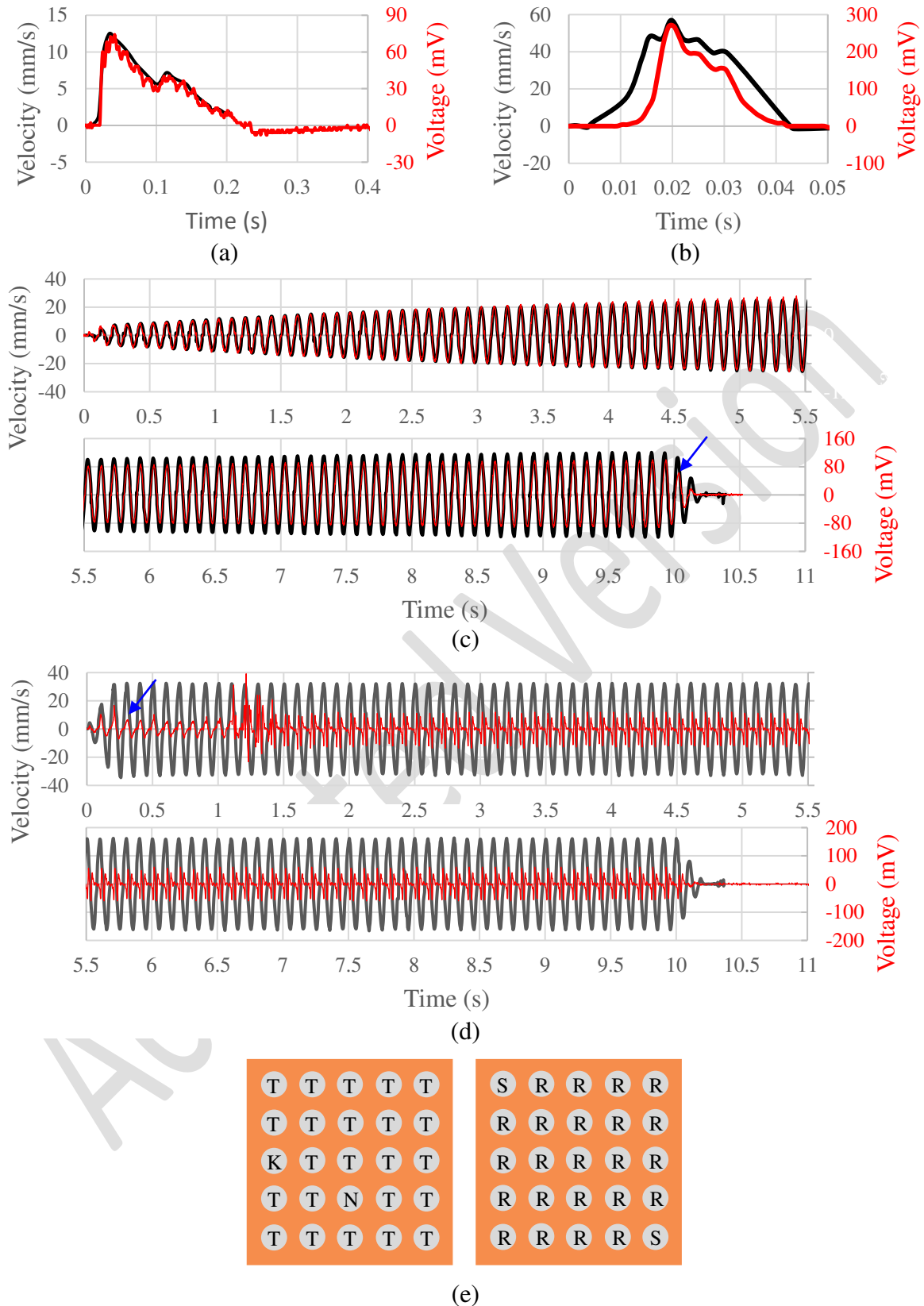
Fig. 8. Sensing results of the (a) mode I and (b) mode II 1-mm steps, and (c) mode I and (d) mode II cyclic steps in the cyclic tests; (e) plot of pin failure, whereby "R" means rupture with partial pull-out from both sides, and "S" rupture with partial pull-out from thin block.
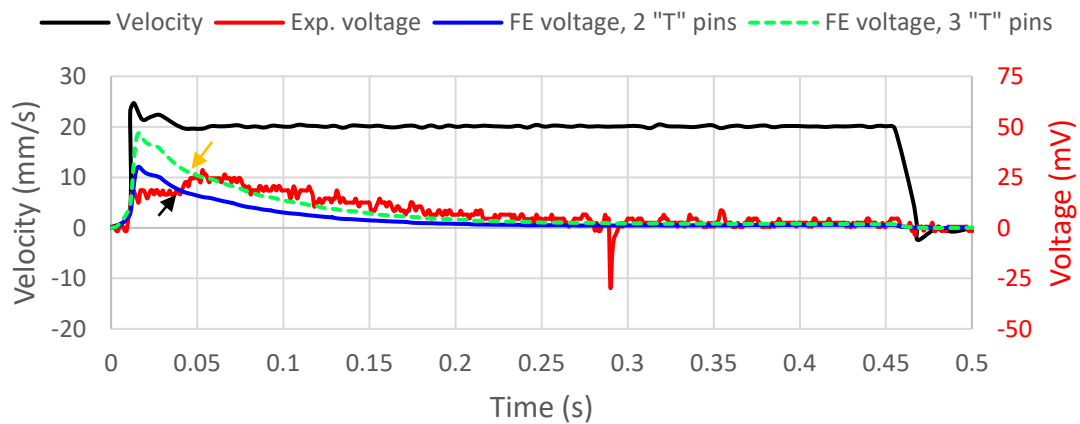
(a)

(b)
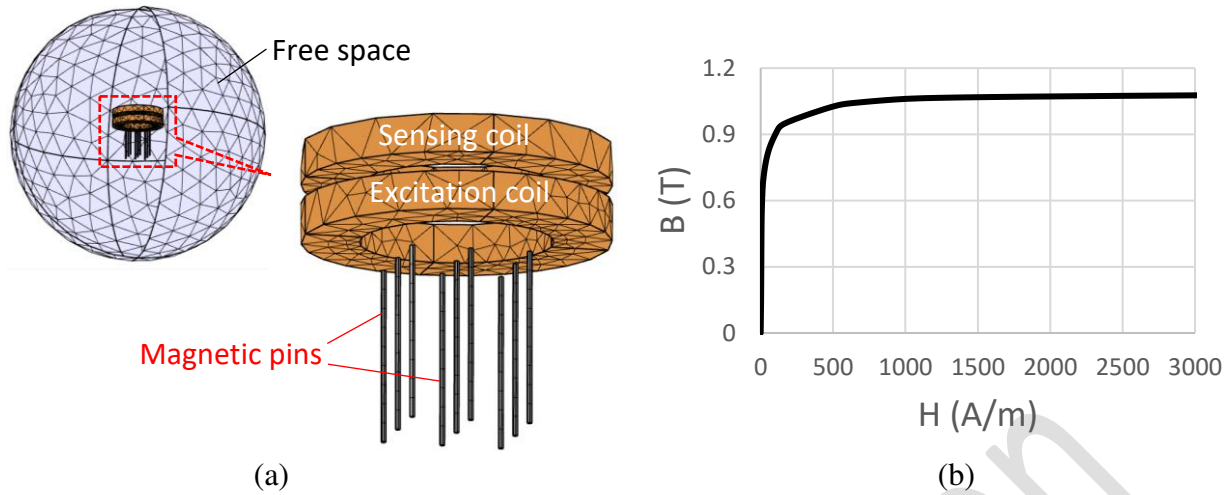
Fig. 9. (a) The "3 × 3" pin model, and (b) the pin material B-H curve used in the FEA [22].
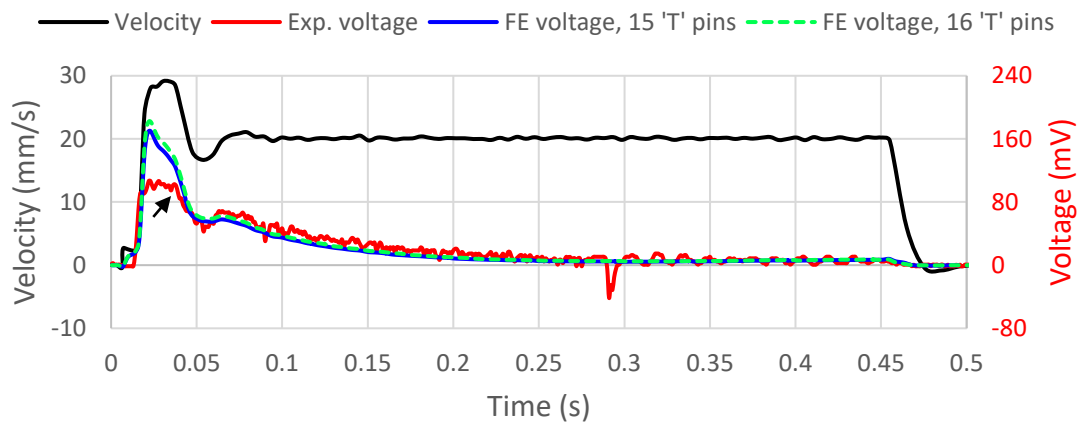


(a)



(b)

Fig. 10. Comparison between model predicted and experiment measured voltage curves for the mode I monotonic (a) "5 × 5" pin and (b) "3 × 3" pin specimens.
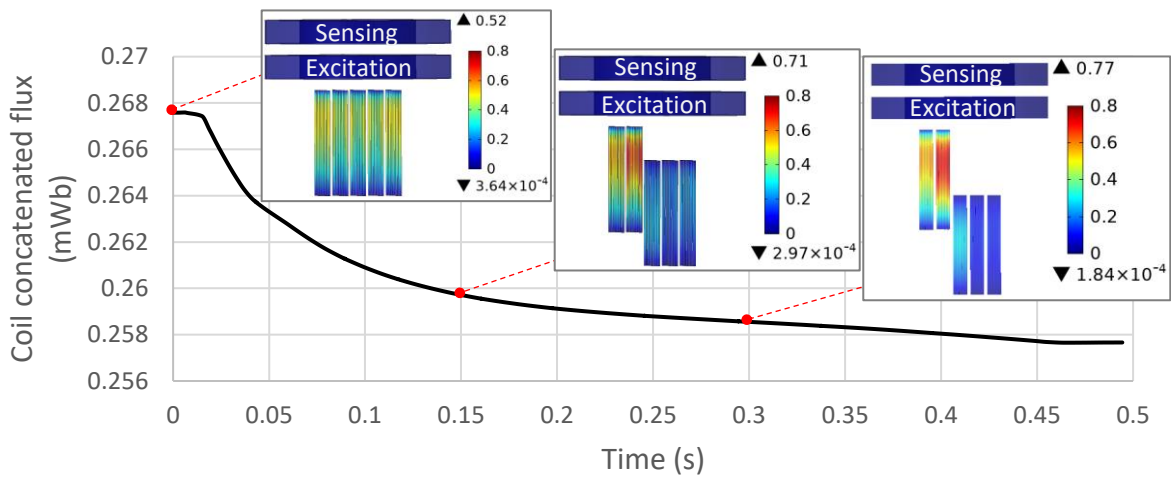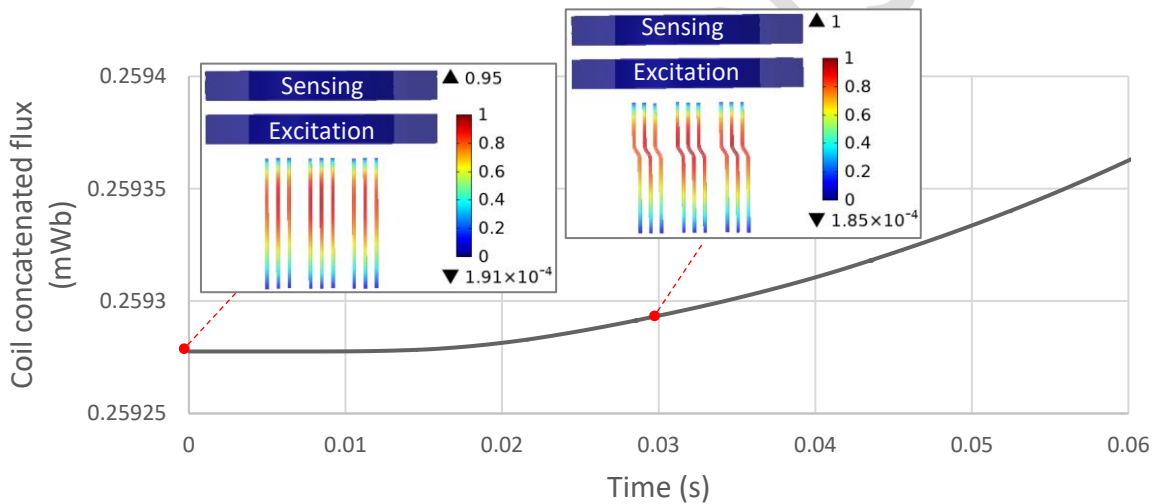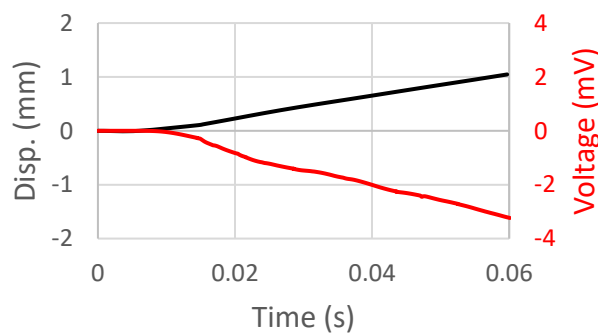
Fig. 11. The magnetic flux concatenated by the sensing coil predicted in the "5×5" pin vertical motion model with 15 "T" pins, with three inset plots corresponding to the magnetic flux density norm inside pins at selected time instants (unit: T).



(a)



(b)

Fig. 12. (a) The sensing coil concatenated flux, with two inset plots for the magnetic flux density norm of the pins at selected time instants (unit: T), and (b) the predicted voltage in the "3×3" pin horizontal motion model under applied displacement up to 1 mm.